



RESEARCH LETTER

10.1029/2018GL078262

Key Points:

- Near-real-time directivity information can be obtained within 17 s using near-field ground motion data variations
- The method could provide a basis to incorporate directivity information in earthquake early warning systems for more accurate shaking alerts
- A prevalence of strong directivity effect is revealed for $M_L \geq 6.0$ earthquakes in Taiwan

Supporting Information:

- Supporting Information S1
- Movie S1
- Movie S2

Correspondence to:

H.-H. Huang,
hhhuang@earth.sinica.edu.tw

Citation:

Jan, J. C., Huang, H.-H., Wu, Y.-M., Chen, C.-C., & Lin, C.-H. (2018). Near-real-time estimates on earthquake rupture directivity using near-field ground motion data from a dense low-cost seismic network. *Geophysical Research Letters*, 45, 7496–7503. <https://doi.org/10.1029/2018GL078262>

Received 13 APR 2018

Accepted 13 JUL 2018

Accepted article online 19 JUL 2018

Published online 8 AUG 2018

Near-Real-Time Estimates on Earthquake Rupture Directivity Using Near-Field Ground Motion Data From a Dense Low-Cost Seismic Network

Jyh Cherng Jan^{1,2} , Hsin-Hua Huang² , Yih-Min Wu^{2,3,4} , Chien-Chih Chen^{1,5}, and Cheng-Hong Lin²

¹Department of Earth Sciences, National Central University, Zhongli, Taiwan, ²Institute of Earth Sciences, Academia Sinica, Taipei, Taiwan, ³Department of Geosciences, National Taiwan University, Taipei, Taiwan, ⁴National Center for Research on Earthquake Engineering, NARLabs, Taipei, Taiwan, ⁵Earthquake-Disaster and Risk Evaluation and Management Center, National Central University, Zhongli, Taiwan

Abstract Rupture directivity of earthquakes could amplify ground shaking and cause serious earthquake hazards. Its timely information is therefore of great importance for early shaking alerts and emergency responses. To this end, we test the feasibility of using near-field (<25 km) ground motion data from a dense low-cost seismic network in Taiwan to constrain directivity information and provide warning for far-field areas. The method is simple and robust, based on the real-time shaking map interpolation and directional attenuation regression analysis. Applications to 16 moderate- to large-magnitude earthquakes in Taiwan and California show that the directivity can be stably obtained within 17 s and agrees well with previous studies when available. An indicator of the strength of directivity amplification is also defined and reveals a prevalence of strong directivity effect for $M_L \geq 6.0$ earthquakes in Taiwan. Such near-real-time directivity information can therefore be useful in earthquake early warning systems for providing more accurate ground shaking alerts.

Plain Language Summary When earthquake rupture propagates in a preferential direction, the ground motions in that direction can be greatly amplified and cause serious earthquake-related damage. The timely knowledge of the rupture direction and possible amplified ground shaking areas is therefore crucial to risk assessment and emergency management. Such information has usually been obtained a few tens of minutes or longer after an earthquake occurs in the past. With short-distance ground motion data from a dense seismic network and real-time data streaming system in Taiwan, we propose a method that can shorten the reporting time to within 17 s after the origin time of the earthquake. This method measures the directional decay of peak ground motions with distance and determines the rupture direction where the ground motions decay least. The difference between the maximum and minimum decaying slopes is used to indicate the strength of directivity amplification and shows a prevalence of strong directivity effect for $M_L \geq 6.0$ earthquakes in Taiwan. Such rapid directivity information is therefore useful for earthquake early warning systems to provide more accurate shaking alerts for distant areas where strong shaking has yet to arrive.

1. Introduction

Strong ground shaking from earthquakes is one of the main factors causing serious damage to buildings, infrastructure, and human lives. When earthquake rupture propagates in a preferential direction (Haskell, 1964), the ground motions in that direction can be greatly amplified and result in unexpected damages and casualties. Such a rupture directivity effect is frequently observed in not only large but also many moderate earthquakes such as the 2009 M_w 6.3 L'Aquila earthquake in Italy (Cirella et al., 2009), the 2014 M_w 6.1 South Napa earthquake in California (Wei et al., 2015), and the 2016 M_w 6.4 Meinong earthquake in Taiwan (M.-H. Huang et al., 2016; Kanamori et al., 2017). How to provide timely information on rupture directivity is therefore of great importance to hazard mitigation and response.

Rupture directivity information can be obtained with various means, such as finite fault inversion (Kikuchi & Kanamori, 1991) and backprojection technique (Ishii et al., 2005) for large earthquakes, and source duration analysis (Tan & Helmberger, 2010), spectral ratio method (Ross & Ben-Zion, 2016), second

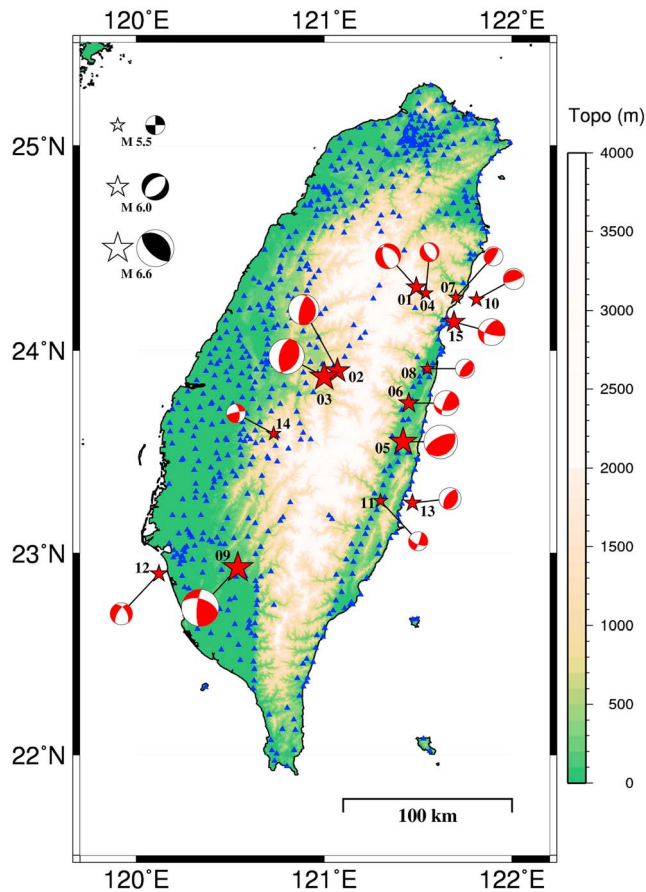


Figure 1. Distribution of *P*-Alert seismic network and used earthquakes. The solid blue triangles denote station locations. The red stars and red focal mechanisms indicate the location and faulting type of 15 $M_L \geq 5.5$ earthquakes used in the study, labeled by the number referred to Table S1. The size of stars is proportional to their local magnitudes. Background color shows the inland topography.

moment method (McGuire et al., 2001), and directivity moment tensor inversion (H.-H. Huang et al., 2017) for small to moderate earthquakes. However, these methods are not ideal for early warning purposes as they often require several tens of minutes or longer to issue the directivity results. Here we propose a method to estimate the directivity using real-time interpolated shaking maps of near-field (<25 km) ground motion data streaming in from a dense low-cost seismic network of early warning system in Taiwan (Hsieh et al., 2014; Wu et al., 2013). We then calculate the slopes of peak ground motion decay (either for peak ground acceleration [PGA] or peak ground velocity [PGV]) from the epicenter in different azimuth and determine the rupture directivity as the azimuth of the maximum slope. This directivity estimation is continuously calculated and updated during the seismic wave propagation until the results stabilize.

We apply the method to 16 moderate- to large-magnitude earthquakes, which are 15 in Taiwan ($M_L \geq 5.5$) and 1 in California ($M_L = 4.7$). The analyses demonstrate that stable results can be obtained within 17 s of earthquake origin time, which can provide timely warning for more distant areas where the strongest ground shaking has yet arrived. Using the azimuthal variations of regression slopes, we investigate the rupture characteristics and quantify the strength of directivity amplification for the events used.

2. *P*-Alert Seismic Network and Data

In Taiwan, a dense seismic network of earthquake early warning (EEW) system, namely, the *P*-Alert network, has gradually been built up since 2012 and contains a total of 636 stations to date (Wu, 2015; Wu et al., 2013). Each seismograph is designed with microelectromechanical system accelerometers (Holland, 2003), which returns three-channel acceleration data in 16 bits blocks with a dynamic range of ± 2 g at a 100-Hz sampling rate. The data are transmitted in real time by internet and the timing control is based on Network Time Protocol synchronization. The *P*-Alert network has successfully been used in many scientific studies including regional (Chen et al., 2015; Wu, 2015) and on-site EEW systems (Hsieh et al.,

2015), near-real-time shaking maps (Hsieh et al., 2014; Wu et al., 2016), and coseismic deformation determination (Jan et al., 2017).

Figure 1 shows the station distribution of *P*-Alert network all around Taiwan. The station spacing is most dense in plain, basin, and low-altitude areas and is relatively sparse in mountainous areas, which are difficult to access and short of power and internet. From January 2013 to February 2018, we select 15 $M_L \geq 5.5$ earthquakes located inland and within 10 km offshore to ensure sufficient azimuthal coverage for rupture directivity analysis (Figure 1 and supporting information Table S1).

3. Method

Our method is based on the real-time data streaming in conjunction with the EEW system of *P*-Alert seismic network. Using the 2016 M_W 6.4 Meinong earthquake as an example (Event 09 in Table S1), when the earthquake occurs, the EEW system is triggered and quickly provides the location of epicenter (Chen et al., 2015; Wu et al., 2013). Meanwhile, the data streaming in are continuously used to calculate peak ground motions of stations and create interpolated shaking maps (Figure 2a). To reduce the effect of radiation pattern while keeping the method simple and fast, three-component seismograms (u_z , u_N , and u_E) are combined into one amplitude seismogram using $\sqrt{u_z^2 + u_N^2 + u_E^2}$ for peak ground motion calculation so that the largest motion could always be retained regardless of wave polarization. Centered at the epicenter location, we then make 36 profiles outward in azimuth per 10° and calculate the slope of peak ground

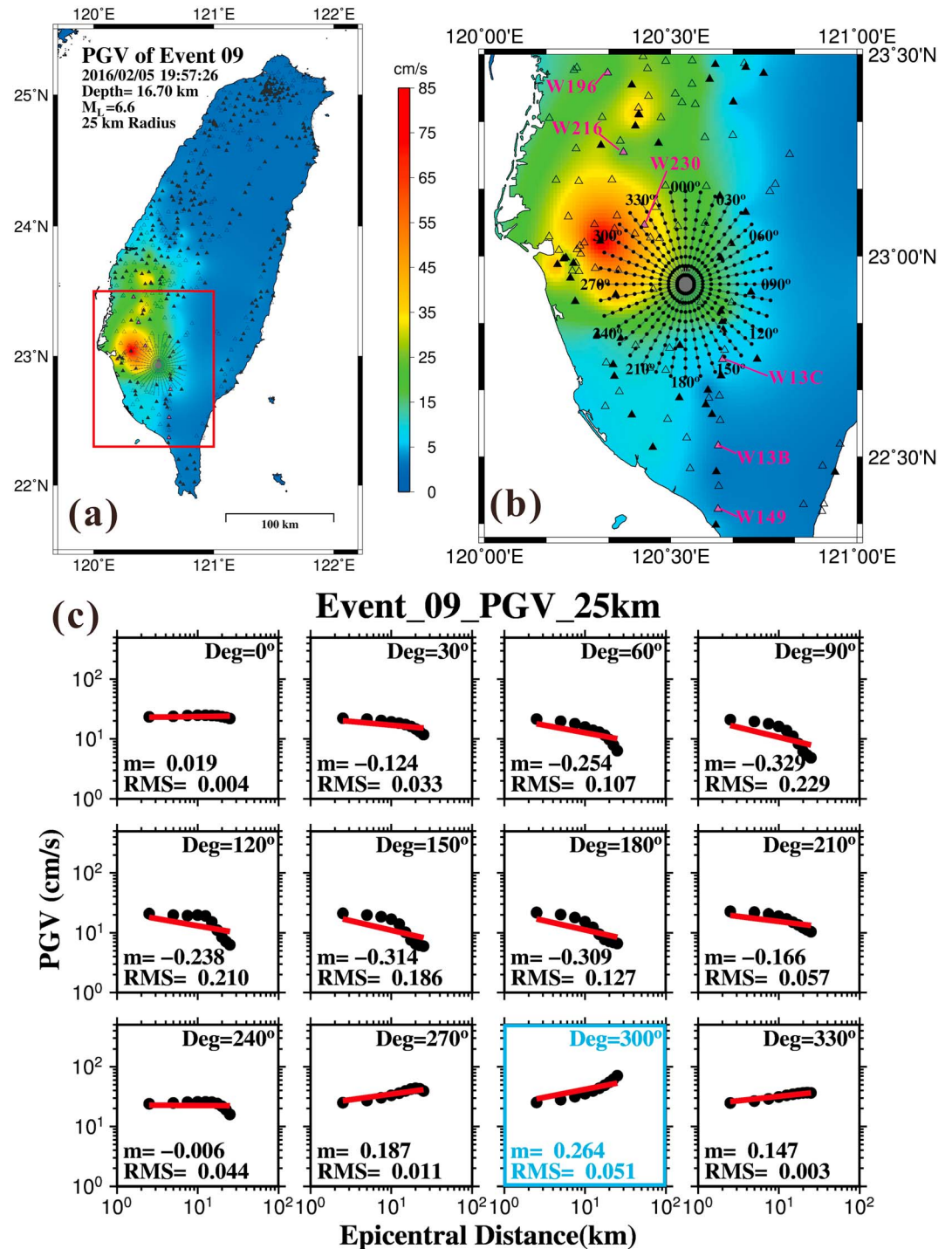


Figure 2. Rupture directivity analysis. (a) PGV shaking map of Event 09, the 2016 Meinong earthquake. The gray lines radiated from epicenter are profiles made for regression analysis and enlarged in (b) as the red box area. Along each profile, the black dots are selected data points to calculate the attenuation relationship between epicentral distance and PGV. Solid and open triangles are used and nonused *P*-Alert stations for interpolating shaking map. The stations marked in red are used in Figure 3b. (c) Regression analysis along the 25-km profiles in azimuth every 30°. Complete regression results are shown in Figure S2. Black dots are data points along each profile, and red lines indicate the fitting lines. The corresponding slope (*m*) and root-mean-square (RMS) are shown in each subplot. The profile of the maximum slope is marked in sky blue. PGV = peak ground velocity.

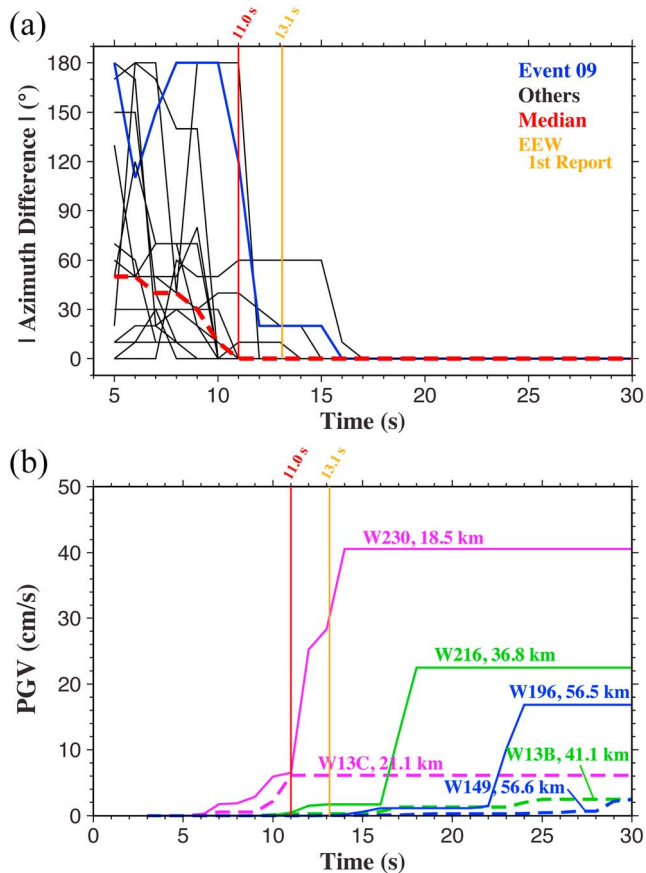


Figure 3. Time-evolving rupture directivity estimates and peak ground velocities at selected stations for Event 09, the 2016 Meinong earthquake. (a) The azimuthal difference of the final rupture directivity estimates and the current estimate at each time step is shown as solid lines for all 15 earthquakes. The blue and black ones indicate the results of Event 09 and others. The red dashed line shows the median results. The solid red line denotes that results of most events become stable after 11 s. The solid yellow line indicates the average first reporting time of earthquake early warning system in Taiwan. (b) Peak ground velocity evolution for the stations at different epicentral distances in the forward direction of rupture directivity are shown in solid pink, green, and blue lines; those for the stations at similar distances but in the backward direction are shown in pink, green, and blue dashed lines correspondingly. The station locations are marked in Figure 2b. The red and yellow lines denote the median convergence time of our directivity estimation and earthquake early warning first report time as in (a). PGV = peak ground velocity.

motion decay along each profile using the simplest attenuation equation accounting only for epicentral distance (R) as follows:

$$\log(A) = \log(A_0) + m \log(R) \quad (1)$$

where A and A_0 are the ground motion data (e.g., PGA or PGV) at targeted sites and epicenter, and m is the slope of regression fitting. The profile length is chosen as 25 km here. We then divide each profile into 10 grid points with regular interval for the regression analysis (blue points in Figure 2b). For earthquakes located close to the coast or on the edge of seismic network, the profile may run over the edge in some directions. In such cases, only profiles with more than four grid points within the edge are used.

Figure 2c shows the regression results between epicentral distance and PGV in azimuth every 30°. Complete regression results (for all 36 directions) are shown in Figure S2. Straightforwardly, the direction of the maximum-slope profile represents the direction of earthquake rupture directivity, which is the positive slope in 300° azimuth in this case. As the interpolated shaking map is updated in time as the number of recording stations increases, the directivity estimation is also updated with time, and it converges after about 16 s for the Meinong earthquake (blue line in Figure 3a and Movie S1).

4. Directivity Estimation and Practice for Early Shaking Alerts

We apply the directivity analysis to all 15 events using PGV data and 25-km profile length, and the results are summarized in Figures S1 and S2. We compare the derived azimuths of rupture directivity with previous studies for the four earthquakes of which the rupture directivity has been reported (Event 02, 03, 05, and 09 in Table S1). They are two 2013 Nantou earthquakes (Lee, 2017; Wen et al., 2014), 2013 Ruisui earthquake (Lee, 2017), and 2016 Meinong earthquake (Jian et al., 2017; Lee, 2017), respectively. The discrepancy of directivity direction between previous studies and this study using different data (e.g., PGV or PGA) and profile lengths (25, 30, and 40 km) are listed in Table S2. In general, using PGV with 25-km profile length gives the best results (our optimal parameters for later analyses), by which the discrepancy is mostly within 10° except Events 05 and 03 with Lee (2017). Note that our estimate of Event 03 is quite consistent with Wen et al. (2014). The directivity directions of Lee (2017) are obtained from the primary slip propagation direction of finite-fault models (not a deterministic directivity estimate), which could possibly result in the relatively large discrepancy observed. For Event 05, its location near the eastern

coastline with relatively poor azimuthal coverage could also contribute to the discrepancy (Figures 1 and S1). In general, our method gives rather satisfactory results considering the resolution of 10° (section 3) and the fast processing speed.

We examine the speed performance of our directivity estimates for early warning practice. Figure 3a shows the time-evolving estimates of directivity analysis for all events since earthquake origin times. For better illustration, we show absolute azimuthal difference between each directivity estimate with the final stable estimate in vertical axis so 0° means the estimates have converged to stable values. Clearly, the azimuthal differences vary a lot in early times but quickly become stable afterward. The median of results converges after 11 s (Figure 3a, red dashed line). In a real situation, the directivity estimation starts from the timing of the first report issued by EEW system. The reporting time of current EEW system is around 13.1 s on average (Chen et al., 2015), so for the events tested here, the directivity reporting time will be between 13.1 and 17 s

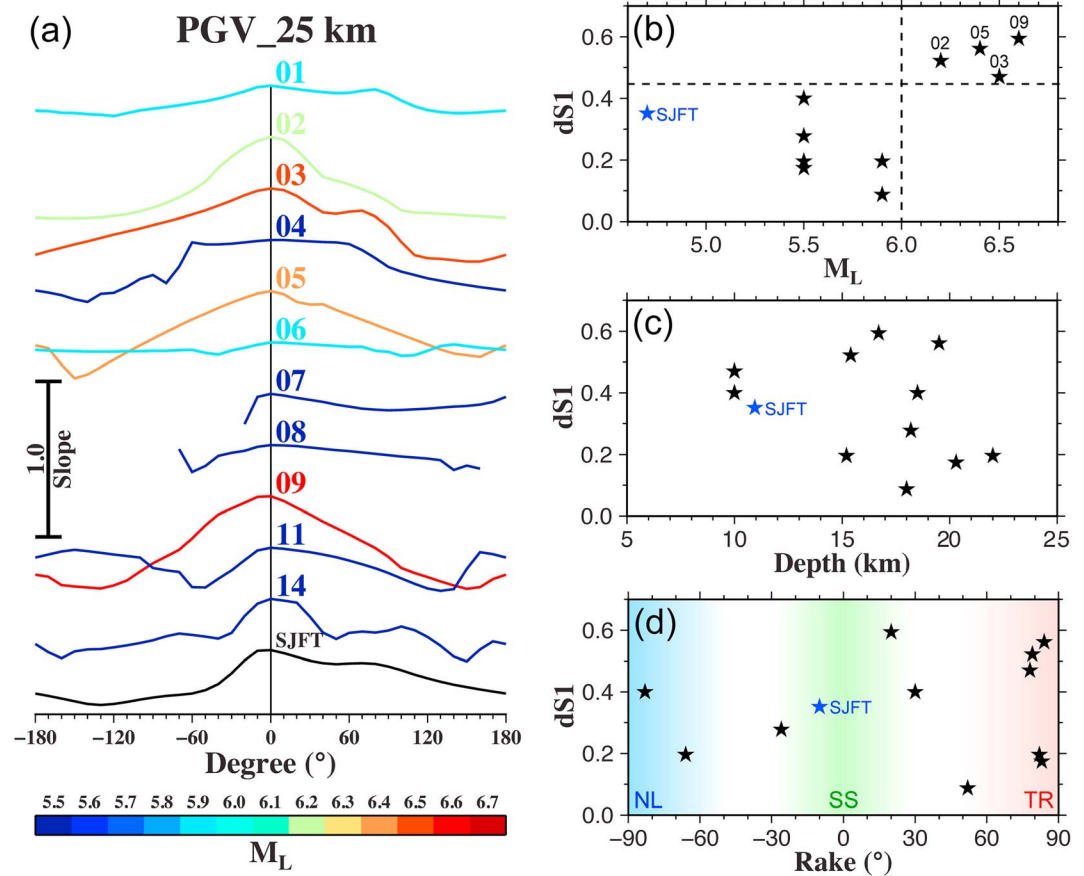


Figure 4. Azimuthal variations of PGV slopes and $dS1$ analysis. (a) The azimuthal variations for the 11 events with gap angles $<180^\circ$ and the San Jacinto fault trifurcation (SJFT) earthquake. Defining the difference between the peak (maximum) and trough (minimum) of the slope variations as $dS1$, its comparisons with the earthquake magnitude, focal depth, and slip rake (faulting type) are shown in (b), (c), and (d), respectively. The black and blue stars indicate the 11 events used and SJFT earthquake. NL, SS, and TR denote normal, strike-slip, and thrust faulting regimes. PGV = peak ground velocity.

(Figure 3a). We note that this reporting time is an ideal estimate and could be slightly longer considering data latency, transmission time, computation time, and so forth in reality. Figure 3b shows the temporal evolution of peak ground motions recorded at six selected stations for Event 09 (Figure 2b), three in the forward direction of rupture directivity and three in the backward direction at comparable epicentral distances. At the time of ~ 13 s, the ground shaking just reaches the peak for Stations W230 and W13C at ~ 20 km. For the stations at ~ 40 km (Stations W216 and W13B) and ~ 56 km (Stations W196 and W149), we can therefore gain lead times of ~ 4 and ~ 11 s for early warning, especially for the areas in the forward direction of rupture directivity where the ground motions will be amplified. The great difference of PGVs at stations in the forward and backward directions demonstrates significant amplification by the directivity effect, although the site effect could also partly contribute.

5. Discussion and Conclusions

We investigate source rupture characteristics using the azimuthal variations of derived PGV regression slopes (Figure 2c) in Figure 4a for the events with gap angle smaller than 180° (11 out of 15). Because we use a constant A_0 for all directions of profiles (equation (1)), the regression slopes derived can essentially be viewed as the relative levels of ground motion amplification at 25 km epicentral distance (excluding source magnitude and distance attenuation already). In this sense, the azimuthal variations can be modeled by a directivity

amplification function C_d (Boatwright, 2007; Convertito et al., 2012) that accounts for both unilateral and bilateral ruptures as

$$C_d = \frac{1}{2} \sqrt{\frac{(1+e)^2}{(1-r_v \cos(\theta))^2} + \frac{(1-e)^2}{(1+r_v \cos(\theta-\varphi))^2}} \quad (2)$$

where $r_v = v_r/v_s$ is a velocity ratio between rupture velocity (v_r) and S wave velocity (v_s) around source area; θ is an angle between the ray taking off the source and the rupture direction; e is a coefficient of percent unilateral rupture, ranging from 0 as a bilateral rupture to 1 as a purely unilateral rupture (Figure S3b); and φ is a deviation angle if the direction of secondary rupture deviates from the backward direction of primary rupture in bilateral rupture cases, $e < 1$ (Figure S3c). Event 02, for example, shows a typical pattern when a unilateral rupture occurs by which the ground motions are amplified most and least in the forward (0°) and backward directions (180° and -180°) of rupture directivity. On the other hand, a number of events exhibit a second peak, such as the peak at 70° for Event 03 and at around backward direction for Events 05 and 11, then indicating a bilateral rupture with another secondary rupture direction. An inversion using spatial variations of ground motion data for the rupture parameters (r_v , e , and φ) may be possible, which is, however, beyond the scope of present study that pursues a fast (and stable) method for early warning application. While many other effects such as site effect are also important, since numerous studies suggested that the most dominant factors on near-field ground motions are rupture directivity and radiation pattern (Imperatoro & Mai, 2013; Mai, 2009; Ripperger et al., 2008), we mainly build the method on a basis that the directivity effect dominates over site effect (and others) at short distances, and the radiation pattern effect has been reduced by taking maximum amplitude of the three components of data (see section 3). To further examine this basis, we apply the method to 11 March 2013 M_w 4.7 San Jacinto fault trifurcation, southern California earthquake that is a purely strike-slip event with strong spatial radiation pattern and in a different tectonic setting (i.e., different site conditions). As shown in Figure S5 and Movie S2, a northwestward directivity can stably be derived within 11 s and shows a good agreement with previous studies (H.-H. Huang et al., 2017; Ross & Ben-Zion, 2016) and the nodal plane of the focal mechanism. The consistency of our directivity estimates with previous studies and the best performance of using shortest 25-km profile length therefore sustain the basis made in the method (Table S1).

Furthermore, we seek an index of rapidly assessing the strength of the directivity effect (and its amplification level) in a near-real-time framework. Given insight from the directivity function modeling (Figure S3), we define two parameters, one is the difference between the maximum (peak) and minimum (trough) slopes ($dS1$); the other is the difference between the slopes in the forward (i.e., maximum) and backward directions ($dS2$). By relating them with the maximum amplification values from the directivity function (Figures S3d–S3f), $dS1$ shows a clear linear trend and is a good indicator for ground motion amplification (Text S1 and Figure S4), while $dS2$ behaves poorly because it can be violated when bilateral rupture occurs and results in a second peak in the backward direction. We show the comparisons between $dS1$ and earthquake magnitude, focal depth, and slip rake (i.e., faulting type) in Figures 4b–4d. Four $M_L \geq 6.0$ earthquakes that caused strong directional ground shaking and certain damage at different levels (Lee, 2017) all show large $dS1$ values above 0.45 (roughly corresponding to 3 times of amplification, Figure S4a). We may roughly set a threshold of $dS1 = 0.45$ for damage earthquakes, although more data will be needed to conclude. On the other hand, no clear relationships are found with the focal depth and faulting type.

An EEW system mainly consists of two components: providing a rapid determination of earthquake location and magnitude using first few seconds of P waves recorded at near-source stations (Allen & Kanamori, 2003; Wu & Kanamori, 2005a, 2005b), and from that, employing ground motion prediction equations (GMPEs) to predict the distribution of PGA, PGV, or intensity for shaking alerts (Allen et al., 2009; Cochran et al., 2017; Wu et al., 2001, 2003). While finite source effect (e.g., rupture directivity) has been known to be an important factor affecting ground motions (Imperatoro & Mai, 2013; Mai, 2009; Ripperger et al., 2008) and has started being considered in many GMPEs in the past two decades (Rowshandel, 2010; Somerville et al., 1997; Spudich & Chiou, 2008), the GMPEs incorporated in EEW are still largely based on point-source assumption since the directivity (and fault extent) could only be assessed after wavefield has been propagating and recorded by the seismic network. That is, the peak ground shaking has already happened. With the near-

real-time estimates of directivity direction and strength ($dS1$) proposed, it may become possible to incorporate directivity-specific GMPEs for more accurate ground shaking prediction in an EEW framework.

We demonstrate that the near-field (<25 km) ground motion data could in theory be used for constraining the earthquake rupture directivity using a simple directional attenuation regression method with an interpolated shaking map. The success of the method proposed largely relies on the availability of a high-density and real-time transmission-capable seismic network. In the case of P -Alert seismic network used here, it generally contains ~14 stations within 25-km radius. One possible limitation may come from the interruption of internet during large earthquakes for near-field stations. As long as not all nearby or one-sided stations cease to function, we expect that the method can still capture the first-order direction of rupture directivity. Recent development of low cost sensors (Cochran et al., 2009; Wu et al., 2013), fiber sensors (Lindsey et al., 2017), and even smartphones (Kong et al., 2016) make the buildup of such dense networks and noninterrupted transmission more feasible nowadays. That would pave the way for the development of real-time-based methods such as ours and others (Bose et al., 2018; Yang et al., 2018) to provide information of rupture directivity and possible amplified ground shaking areas as fast as possible for hazard mitigation and emergency management.

Acknowledgments

We thank Chun-Hsiang Kuo for helpful discussion. We also thank the editor Gavin Hayes and two anonymous reviewers for their constructive comments which substantially improve the work. All event waveform data used in this study can be downloaded from the Ftp site (<ftp://ftp.p-alert.tw:2121/events>) maintained by earthquake early warning (EEW) research group at the National Taiwan University. This work was funded by a Ministry of Science and Technology grant 105-2116-M-001-026-MY2.

References

- Allen, R. M., Gasparini, P., Kamigaiichi, O., & Bose, M. (2009). The status of earthquake early warning around the world: An introductory overview. *Seismological Research Letters*, 80(5), 682–693. <https://doi.org/10.1785/gssrl.80.5.682>
- Allen, R. M., & Kanamori, H. (2003). The potential for earthquake early warning in southern California. *Science*, 300(5620), 786–789. <https://doi.org/10.1126/science.1080912>
- Boatwright, J. (2007). The persistence of directivity in small earthquakes. *Bulletin of the Seismological Society of America*, 97, 1850–1861. *Seismological Research Letters*, 80(5), 682–693. <https://doi.org/10.1785/gssrl.80.5.682>
- Bose, M., Smith, D. E., Felizardo, C., Meier, M.-A., Heaton, T. H., & Clinton, J. F. (2018). FinDer v.2: Improved real-time ground-motion predictions for $M2$ – $M9$ with seismic finite-source characterization. *Geophysical Journal International*, 212(1), 725–742. <https://doi.org/10.1093/gji/ggx430>
- Chen, D.-Y., Wu, Y.-M., & Chin, T.-L. (2015). Incorporating low-cost seismometers into the Central Weather Bureau seismic network for earthquake early warning in Taiwan. *Terrestrial, Atmospheric and Oceanic Sciences*, 26(5), 503–513. [https://doi.org/10.3319/TAO.2015.04.17.01\(T\)](https://doi.org/10.3319/TAO.2015.04.17.01(T))
- Cirella, A., Piatanesi, A., Cocco, M., Tinti, E., Scognamiglio, L., Michelini, A., et al. (2009). Rupture history of the 2009 L'Aquila (Italy) earthquake from non-linear joint inversion of strong motion and GPS data. *Geophysical Research Letters*, 36, L19304. <https://doi.org/10.1029/2009GL039795>
- Cochran, E. S., Kohler, M. D., Given, D. D., Guiwits, S., Andrews, J., Meier, M.-A., et al. (2017). Earthquake early warning ShakeAlert system: Testing and certification platform. *Seismological Research Letters*, 89(1), 108–117. <https://doi.org/10.1785/0220170138>
- Cochran, E. S., Lawrence, J. F., Christensen, C., & Jukka, R. S. (2009). The quake-catcher network: Citizen science expanding seismic horizons. *Seismological Research Letters*, 80(1), 26–30. <https://doi.org/10.1785/gssrl.80.1.26>
- Convertito, V., Caccavale, M., De Matteis, R., Emolo, A., Wald, D., & Zollo, A. (2012). Fault extent estimation for near-real-time ground-shaking map computation purposes. *Bulletin of the Seismological Society of America*, 102(2), 661–679. <https://doi.org/10.1785/0120100306>
- Haskell, N. A. (1964). Total energy and energy spectral density of elastic wave radiation from propagating faults. *Bulletin of the Seismological Society of America*, 54, 1811–1841.
- Holland, A. (2003). Earthquake data recorded by the MEMS accelerometer: Field testing in Idaho. *Seismological Research Letters*, 74(1), 20–26. <https://doi.org/10.1785/gssrl.74.1.20>
- Hsieh, C.-Y., Chao, W.-A., & Wu, Y.-M. (2015). An examination of the threshold-based earthquake early warning approach using a low cost seismic network. *Seismological Research Letters*, 86(6), 1664–1667. <https://doi.org/10.1785/0220150073>
- Hsieh, C.-Y., Wu, Y.-M., Chin, T.-L., Kuo, K.-H., Chen, D.-Y., Wang, K.-S., et al. (2014). Low cost seismic network practical applications for producing quick shaking maps in Taiwan. *Terrestrial, Atmospheric and Oceanic Sciences*, 25(5), 617–624. [https://doi.org/10.3319/TAO.2014.03.27.01\(T\)](https://doi.org/10.3319/TAO.2014.03.27.01(T))
- Huang, H.-H., Aso, N., & Tsai, V. C. (2017). Toward automated directivity estimates in earthquake moment tensor inversion. *Geophysical Journal International*, 211(2), 1062–1076. <https://doi.org/10.1093/gji/ggx354>
- Huang, M.-H., Tung, H., Fielding, E. J., Huang, H.-H., Liang, C., Huang, C., & Hu, J.-C. (2016). Multiple fault slip triggered above the 2016 M_w 6.4 Meinong earthquake in Taiwan. *Geophysical Research Letters*, 43, 7459–7467. <https://doi.org/10.1002/2016GL069351>
- Imperatori, W., & Mai, P. M. (2013). Broad-band near-field ground motion simulations in 3-dimensional scattering media. *Geophysical Journal International*, 192(2), 725–744. <https://doi.org/10.1093/gji/ggs041>
- Ishii, M., Shearer, P. M., Houston, H., & Vidale, J. E. (2005). Extent, duration and speed of the 2004 Sumatra-Andaman earthquake imaged by the Hi-Net array. *Nature*, 435(7044), 933–936. <https://doi.org/10.1038/nature03675>
- Jan, C. J., Chao, W.-A., Wu, Y.-M., Chen, C.-C., & Lin, C.-H. (2017). How well can we extract the permanent displacement from low-cost MEMS accelerometers? *Sensors*, 17(11), 2643. <https://doi.org/10.3390/s17112643>
- Jian, P.-R., Hung, S.-H., Meng, L., & Sun, D. (2017). Rupture characteristics of the 2016 Meinong earthquake revealed by the back projection and directivity analysis of teleseismic broadband waveforms. *Geophysical Research Letters*, 44(8), 3545–3553. <https://doi.org/10.1002/2017GL072552>
- Kanamori, H., Ye, L., Huang, B.-S., Huang, H.-H., Lee, S.-J., Liang, W.-T., et al. (2017). A strong-motion hot spot of the 2016 Meinong, Taiwan, earthquake ($M_w = 6.4$). *Terrestrial, Atmospheric and Oceanic Sciences*, 28. <https://doi.org/10.3319/TAO.2016.10.07.01>
- Kikuchi, M., & Kanamori, H. (1991). Inversion of complex body waves—III. *Bulletin of the Seismological Society of America*, 81, 2335–2350.
- Kong, Q., Allen, R. M., & Schreier, L. (2016). MyShake: Initial observations from a global smartphone seismic network. *Geophysical Research Letters*, 43, 9588–9594. <https://doi.org/10.1002/2016GL070955>

- Lee, S.-J. (2017). Lessons learned from source rupture to strong ground motion simulations: An example from Taiwan. *Bulletin of the Seismological Society of America*, 107(5), 2106–2116. <https://doi.org/10.1785/0120170030>
- Lindsey, N. J., Martin, E. R., Dreger, D. S., Freifeld, B., Cole, S., James, S. R., et al. (2017). Fiber-optic network observations of earthquake wavefields. *Geophysical Research Letters*, 44, 11,792–11,799. <https://doi.org/10.1002/2017GL075722>
- Mai, P. M. (2009). Ground-motion complexity and scaling in the near-field of earthquake ruptures. In W. Lee, & R. Meyers (Eds.), *Encyclopedia of complexity and system sciences*, (pp. 4435–4474). New York: Springer.
- McGuire, J. J., Zhao, L., & Jordan, T. H. (2001). Measuring the second degree moments of earthquake space-time distributions. *Geophysical Journal International*, 145(3), 661–678. <https://doi.org/10.1046/j.1365-246x.2001.01414.x>
- Ripperger, J., Mai, P. M., & Ampuero, J.-P. (2008). Variability of near-field ground motion from dynamic earthquake rupture simulations. *Bulletin of the Seismological Society of America*, 98(3), 1207–1228. <https://doi.org/10.1785/0120070076>
- Ross, Z. E., & Ben-Zion, Y. (2016). Toward reliable automated estimates of earthquake source properties from body wave spectra. *Journal of Geophysical Research*, 121, 4390–4407. <https://doi.org/10.1002/2016JB013003>
- Rowshandel, B. (2010). Directivity correction for the next generation attenuation (NGA) relations. *Earthquake Spectra*, 26(2), 525–559. <https://doi.org/10.1193/1.3381043>
- Somerville, P. G., Smith, N. F., Graves, R. W., & Abrahamson, N. A. (1997). Modification of empirical strong ground motion attenuation relations to include the amplitude and duration effects of rupture directivity. *Seismological Research Letters*, 68(1), 199–222. <https://doi.org/10.1785/gssrl.68.1.199>
- Spudich, P., & Chiou, B. S. J. (2008). Directivity in NGA earthquake ground motions: Analysis using isochrone theory. *Earthquake Spectra*, 24(1), 279–298. <https://doi.org/10.1193/1.2928225>
- Tan, Y., & Helmberger, D. (2010). Rupture directivity of the 2003 Big Bear sequence. *Bulletin of the Seismological Society of America*, 100(3), 1089–1106. <https://doi.org/10.1785/0120090074>
- Wei, S., Barbot, S., Graves, R., Lienkaemper, J. J., Wang, T., Hudnut, K., et al. (2015). The 2014 M_w 6.1 South Napa earthquake: A unilateral rupture with shallow asperity and rapid afterslip. *Seismological Research Letters*, 86(2A), 344–354. <https://doi.org/10.1785/0220140249>
- Wen, Y.-Y., Miyake, H., Yen, Y.-T., Irikura, K., & Ching, K.-E. (2014). Rupture directivity effect and stress heterogeneity of the 2013 Nantou blind-thrust earthquakes, Taiwan. *Bulletin of the Seismological Society of America*, 104(6), 2933–2942. <https://doi.org/10.1785/0120140109>
- Wu, Y.-M. (2015). Progress on development of an earthquake early warning system using low-cost sensors. *Pure and Applied Geophysics*, 172(9), 2343–2351. <https://doi.org/10.1007/s00024-014-0933-5>
- Wu, Y.-M., Chen, D.-Y., Lin, T.-L., Hsieh, C.-Y., Chin, T.-L., Chang, W.-Y., et al. (2013). A high-density seismic network for earthquake early warning in Taiwan based on low cost sensors. *Seismological Research Letters*, 84(6), 1048–1054. <https://doi.org/10.1785/0220130085>
- Wu, Y.-M., & Kanamori, H. (2005a). Experiment on an onsite early warning method for the Taiwan early warning system. *Bulletin of the Seismological Society of America*, 95(1), 347–353. <https://doi.org/10.1785/0120040097>
- Wu, Y.-M., & Kanamori, H. (2005b). Rapid assessment of damage potential of earthquakes in Taiwan from the beginning of P waves. *Bulletin of the Seismological Society of America*, 95(3), 1181–1185. <https://doi.org/10.1785/0120040193>
- Wu, Y.-M., Liang, W.-T., Mittal, H., Chao, W.-A., Lin, C.-H., Huang, B.-S., & Lin, C.-M. (2016). Performance of a low-cost earthquake early warning system (P-Alert) during the 2016 M_L 6.4 Meinong (Taiwan) earthquake. *Seismological Research Letters*, 87(5), 1050–1059. <https://doi.org/10.1785/0220160058>
- Wu, Y.-M., Shin, T.-C., & Chang, C.-H. (2001). Near real-time mapping of peak ground acceleration and peak ground velocity following a strong earthquake. *Bulletin of the Seismological Society of America*, 91, 1218–1228.
- Wu, Y.-M., Teng, T.-L., Shin, T.-C., & Hsiao, N.-C. (2003). Relationship between peak ground acceleration, peak ground velocity, and intensity in Taiwan. *Bulletin of the Seismological Society of America*, 93(1), 386–396. <https://doi.org/10.1785/0120020097>
- Yang, B. M., Huang, T.-C., & Wu, Y.-M. (2018). ShakingAlarm: A nontraditional regional earthquake early warning system based on time-dependent anisotropic peak ground-motion attenuation relationships. *Bulletin of the Seismological Society of America*, 108(3A), 1219–1230. <https://doi.org/10.1785/0120170105>